ANNALS OF GEOPHYSICS, 69, 2, SA219, 2026; doi:10.4401/ag-9470
OPEN ACCESS

Comparison of Sporadic-E Characteristics from coincident COSMIC-2 Radio Occultation and Digisonde Observations

Mefe Moses[*,1], Haris Haralambous[2,3], Wilberforce Muniafu[4], Mostafa Hegy[5], Nahum Maundu[6], Kisembo Francis[7]

(1) Ahmadu Bello University Zaria, Department of Geomatics, Kaduna, Nigeria
(2) Frederick Research Center, Nicosia, Cyprus
(3) Frederick University, Department of Electrical and Computer Engineering and Informatics, Nicosia, Cyprus
(4) Masinde Muliro University of Science and Technology, Kenya
(5) National Research Institute of Astronomy and Geophysics, Geomagnetic and Geoelectric Department, Cairo, Egypt
(6) Pwani University, Kilifi, Kenya
(7) Mbarara University of Science and Technology, Mbarara, Uganda

Article history: received October 29, 2025; accepted April 18, 2026

Abstract

Sporadic-E (Es) layers are thin, transient layers that influence radio propagation. Recently there has been growing interest in global Es occurrence modelling which is also relevant to the International Reference Ionosphere (IRI) model that is currently lacking a model component for Es occurrence. This study presents a comprehensive intercomparison of Es layer altitude and intensity from coincident COSMIC-2 GNSS radio-occultation (RO) and Digisonde observations during 2020-2023. Using strict spatial (±2°) and temporal (±10 min) collocation, 4,367 quality-controlled RO-Digisonde profile pairs from 19 globally distributed stations were analysed. Es peak altitude (RO geometric height hRO vs Digisonde virtual height h′Es) shows weak-to-moderate station-wise linear agreement (Pearson R ≈ 0.22-0.66) and root-mean-square differences of ≈4.2-7.8 km (multi-station mean ≈6 km), indicating that COSMIC-2 reproduces the broad statistical distribution of Es altitudes while instantaneous, site-to-site agreement varies. Intensity comparisons (RO L1 amplitude scintillation index S4 vs Digisonde blanketing frequency, fbEs), evaluated for RO-detected Es events with S4 > 0.2, reveal a consistently positive but generally modest relationship (R up to ≈0.36), with statistically significant agreement at 14 of 19 stations and strongest correlations at equatorial and some low-latitude sites. Even at the best locations, fbEs explains at most ~13% of S4 variance, underscoring the influence of small-scale structuring, differing physical sensitivities, sampling geometry, and collocation uncertainty on scintillation responses. These results quantify the complementarities and limitations of RO and ionosonde Es metrics and provide a benchmark assessment for their use in future monitoring systems and empirical modelling.

Keywords: Sporadic-E; Radio occultation; COSMIC-2; Digisonde; Blanketing frequency; Amplitude scintillation

1. Introduction

Sporadic E (Es) layers are transient, thin sheets of enhanced electron density formed by long-lived metallic ions of meteoric origin (e.g., Fe^+, Mg^+) converged by neutral winds (Mathews, 1998; Whitehead, 1961) and intensify in the ionospheric E region (~90-130 km). Their climatology is characterized by seasonal, diurnal, and latitudinal features. Es occurrence and intensity maximize during daytime in the summer hemisphere at midlatitudes, decrease toward winter, and are comparatively sparse near the magnetic equator (Arras et al., 2008; Hodos et al., 2022; Resende et al., 2018). Because Es layers are thin (often <5 km) and laterally extended (tens to hundreds of kilometres) they can give rise to vertical gradients in electron density which affect radio propagation, reflecting HF/VHF signals and introduce GNSS amplitude and phase scintillation that can degrade positioning, navigation, and timing (Emmons et al., 2023; Moro et al., 2025; Yu et al., 2019).

The established physical framework for midlatitude Es behaviour is the wind-shear theory, which explains the formation of thin metallic ion layers at altitudes where the vertical shear of the horizontal neutral wind is negative, typically in response to diurnal and semidiurnal tides (Axford and Cunnold, 1966; Haldoupis, 2012). At low latitudes and near the magnetic equator, the horizontal geomagnetic field reduces the effectiveness of this convergence mechanism. Here, electrodynamic processes associated with the equatorial electrojet and gradient drifts can influence or interact with wind shear, forming broad, blanketing layers that peak at higher altitudes (Arras et al., 2022; Luo et al., 2021; Resende et al., 2018). Numerical simulations demonstrate that coupling between large-scale winds and plasma instabilities shapes the structure of Es layers and drives the development of small-scale gradients relevant to scintillation (Didebulidze and Lomidze, 2008; Yokoyama et al., 2009). At high latitudes, Es formation can also be affected by convective electric field structures, further contributing to the diversity of generation mechanisms (Mathews, 1998).

Historically, ionosondes have been the primary instruments for monitoring key Es characteristics, including the critical frequency foEs (a proxy for peak electron density), the blanketing frequency (fbEs), and the virtual height h′Es (Haldoupis, 2012; Mathews, 1998). Decades of ionosonde observations established the basic global morphology and tidal/seasonal variation (e.g., Merriman et al., 2021). However, ionosonde coverage is sparse over oceans and much of the Southern Hemisphere, limiting global coverage. Recent advances in ionosonde processing have also refined the derivation of Es parameters, reducing daytime biases and yielding improved estimates of layer height and metal-ion related frequencies, which enhances the utility of ionosonde datasets for comparative studies (Haldoupis et al., 2025). Over the past two decades, GNSS radio occultation has revolutionized global Es monitoring. Low Earth orbit (LEO) receivers measure refractivity and amplitude/phase fluctuations along slant ray paths, allowing the detection of sharp E-region gradients associated with Es layers with high vertical resolution and near-uniform global coverage (Arras et al., 2008; Igarashi et al., 2001; Wickert et al., 2004; Wu et al., 2005). FORMOSAT-3/COSMIC, and more recently COSMIC-2, provide thousands of daily radio occultation profiles, enabling robust characterization of global Es occurrence patterns (Arras et al., 2008; Arras et al., 2022; Chu et al., 2014; Hodos et al., 2022; Swarnalingam et al., 2020).

There is growing interest in developing global Es occurrence and intensity models based primarily on the extensive GNSS radio occultation (RO) databases, both to characterize climatology and to support operational ionospheric products. The International Reference Ionosphere (IRI), as the community standard empirical specification of ionospheric parameters, has highlighted the need for improved Es climatology and explicitly identified incorporation of Es occurrence and intensity based on large RO datasets as a priority for future versions (Niu and Fang, 2023; Yu et al., 2020). Within this context, the fbEs, which represents the maximum frequency at which the Es layer completely masks reflections from the underlying ionosphere, is of particular interest because it characterizes the uniformly distributed component of the Es metal ion plasma and is widely used as an ionosonde based intensity metric (Haldoupis et al., 2025; Merriman et al., 2021; Niu et al., 2019).

To support fbEs based modelling, several comparison studies have exploited both RO and ionosonde datasets to investigate the complementarity of these techniques and to quantify systematic biases. Ionosondes provide direct measurements of Es plasma frequency parameters (foEs, fbEs, h′Es), with continuous local time coverage at fixed locations, whereas RO senses integrated refractivity gradients along an extended tangent path and is intrinsically sensitive to thin, vertically localized structures (Haldoupis et al., 2023; Niu and Fang, 2023; Niu et al., 2019; Yu et al., 2020). Intercomparison studies show that RO and ionosondes recover broadly consistent climatologies of Es occurrence, altitude, and seasonal/diurnal behaviour, but exhibit systematic differences in detection thresholds and absolute intensities arising from instrumental sensitivity, geometry, and analysis methodology (Emmons et al., 2022;

Haldoupis et al., 2023; Niu et al., 2019; Yu et al., 2020). In particular, global Digisonde statistics reveal that fbEs occurrence rates are substantially lower than foEs rates, and the foEs/fbEs occurrence rate ratio increases sharply with intensity threshold, indicating that fbEs selectively samples the strongest blanketing events (Niu et al., 2019).

These methodological contrasts and the different physical content of the observables help explain the generally weak linear relationships reported between RO derived intensity or scintillation indices (e.g., S4, Smax) and ionosonde parameters. While foEs reflects the peak electron density, fbEs is more closely tied to the uniform blanketing component of the Es layer, and both quantities differ fundamentally from the small scale gradient and irregularity spectrum that controls RO scintillation (Emmons et al., 2022; Haldoupis et al., 2025; Yu et al., 2020). Consequently, layers with high fbEs but relatively smooth structure can produce only modest amplitude scintillation, whereas layers with moderate fbEs but intense small scale structuring can generate strong S4 (Emmons et al., 2022; Haldoupis et al., 2023; Haldoupis et al., 2025).

Previous work further shows that the degree of agreement between RO based and ionosonde based Es analysis depends on season, local time, latitude, and the specific intensity/occurrence criteria applied, including fbEs thresholds (Niu and Fang, 2023; Niu et al., 2019; Yu et al., 2020). RO provides dense global sampling and has been used to derive empirical models of Es intensity and occurrence, while ionosondes remain the primary "ground truth" for defining robust fbEs based occurrence rates and intensity benchmarks (Haldoupis et al., 2023; Niu and Fang, 2023; Niu et al., 2019; Yu et al., 2020). Updated global fbEs and foEs occurrence statistics from the GIRO Digisonde network now provide a critical reference for mapping RO derived occurrence metrics to specific ionosonde intensity thresholds (e.g., fbEs $\geq$3 MHz) and for reconciling the factor of several spread among different RO based Es occurrence climatologies (Niu et al., 2019).

Two recent methodological advances are especially pertinent to fbEs. First, improved ionosonde parameters foμEs and fbμEs have been introduced to remove long standing daytime biases caused by ambient E region photoionization, thereby isolating the true metal ion component of Es intensity (Haldoupis et al., 2025; Merriman et al., 2021). These corrections reduce systematic overestimation of both foEs and fbEs during sunlit hours by ~30-50% and ~40%, respectively, and are strongly recommended for both research and operational applications (Haldoupis et al., 2025). Second, inversion and machine learning approaches using paired RO-ionosonde datasets have demonstrated that RO amplitude and phase perturbations can be used to retrieve Es intensity parameters with operational accuracy, providing a pathway to global fbEs related proxies from spaceborne platforms (Emmons et al., 2022; Niu and Fang, 2023; Yu et al., 2020). Complementary 3-D tomography and dense ground based GNSS networks further resolve the horizontal structuring and dynamics of strong Es, offering context for short term discrepancies between collocated ionosonde and RO measurements (Haldoupis et al., 2023). Unlike earlier RO-ionosonde intercomparisons that were largely confined to occurrence statistics, foEs-based intensity metrics, or limited regional case studies, this study presents a globally distributed, station-wise benchmarking analysis of sporadic-E altitude and intensity using collocated COSMIC-2 and Digisonde observations collected during the early operational phase of COSMIC-2. The analysis is explicitly formulated around the fbEs, the operationally relevant descriptor of strong blanketing layers, and directly quantifies its statistical relationship with RO-derived L-band scintillation (S4). The primary aim is to characterise agreement between the two measurement systems under consistent collocation and quality-control criteria, and to provide a comparative reference for future climatological and modelling studies rather than to claim new sporadic-E physics or an operational data-assimilation framework.

2. Materials and Methods

We analysed coincident COSMIC-2 RO and Digisonde measurements collected between 2020 and 2023 from 19 Digisonde stations. The dataset comprises 4367 matched RO-Digisonde profiles. These paired observations form the basis for comparing sporadic-E layer parameters derived from the two techniques.

2.1 Digisonde Data Acquisition and Processing

Digisonde ionograms for each station were sourced from the corresponding station databases and processed using the SAO-Explorer (Standard Archiving Output) software developed by the University of Massachusetts Lowell (https://ulcar.uml.edu/SAO-X/SAO-X.html). Automated scaling can misinterpret sporadic-E (Es), especially

for weaker Es layers at higher altitudes (>130 km), therefore, all ionograms were manually scaled by experts to ensure accurate retrieval of the Es characteristics. The Digisonde Es altitude parameter used in all comparisons is h′Es, obtained from manual ionogram scaling. The parameter h′Es is defined as the minimum virtual height of the sporadic-E trace at its maximum observable frequency, corresponding to the virtual reflection height of the strongest portion of the Es layer. We implemented a systematic quality-control procedure to improve reliability. Ionograms affected by excessive noise or ambiguous echoes were flagged for review, and those with unresolved or internally inconsistent interpretations were either discarded. Figure 1 shows the geographical distribution of the stations, while Table 1 provides the summary of Digisonde stations included in this study. Stations are classified as equatorial (±0°-10°), low-latitude (±10°-30°), and mid-latitude (±30°-60°) following standard ionospheric conventions.

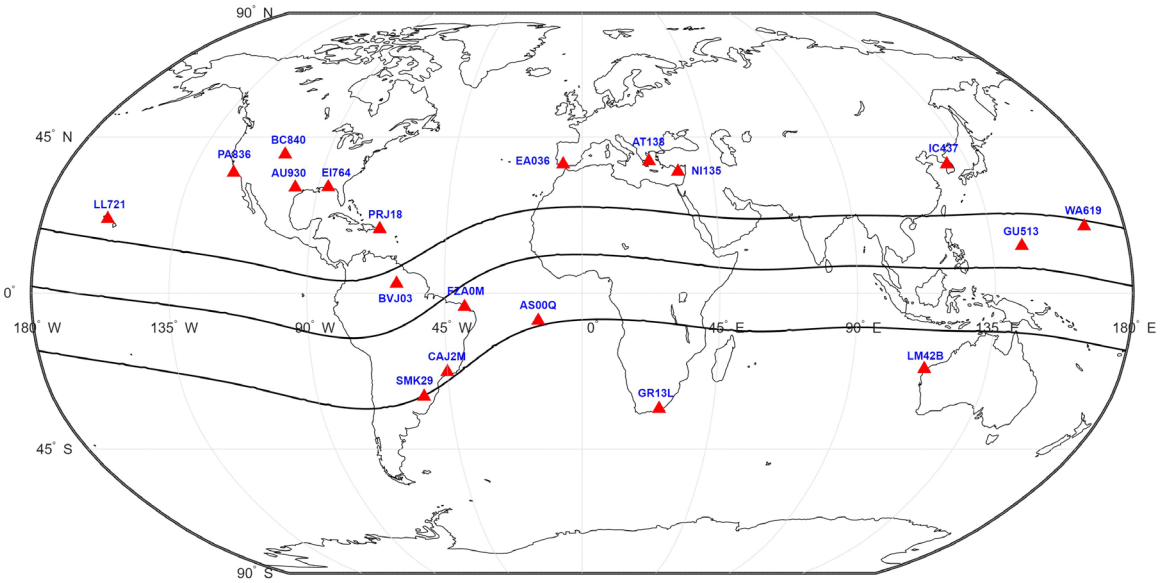

Figure 1. Geographic distribution of ionosonde (Digisonde) stations utilized in this study.

Table 1. Summary of Digisonde stations included in this study.

S/No.	Station	Country	Location	System Type	Latitude (°)	Longitude (°)
1.	AS00Q	USA (Ascension Island)	Ascension Island	DPS4D	−7.95	345.6
2.	AT138	Greece	Athens	DPS4D	38	23.5
3.	AU930	USA	Austin, TX	D256	30.4	262.3
4.	BC840	USA	Boulder, CO	D256	40	254.7
5.	BVJ03	Brazil	Boa Vista	DPS4D	2.8	299.3
6.	CAJ2M	Brazil	Cachoeira Paulista	DPS4D	−22.7	315
7.	EA036	Spain	El Arenosillo	DPS4D	37.1	353.3
8.	EI764	USA (Eglin AFB)	Eglin AFB, FL	DPS4D	30.5	273.5
9.	FZA0M	Brazil	Fortaleza	DPS4	−3.9	321.6

S/No.	Station	Country	Location	System Type	Latitude (°)	Longitude (°)
10.	GR13L	South Africa	Grahamstown	DPS4D	−33.3	26.5
11.	GU513	USA (Guam)	Guam	DPS4D	13.62	144.86
12.	IC437	South Korea	I-Cheon	DPS4D	37.14	127.54
13.	LL721	USA (Lualualei)	Lualualei	DPS4D	21.43	201.85
14.	LM42B	Australia	Learmonth	DPS4D	−21.8	114.1
15.	NI135	Cyprus	Nicosia	DPS4D	35.03	33.16
16.	PA836	USA	Point Arguello, CA	D256 DISS	34.7	239.4
17.	PRJ18	USA (Puerto Rico)	Ramey, PR	D256 DISS	18.5	292.9
18.	SMK29	Brazil	Santa Maria	DPS4D	−29.73	306.29
19.	WA619	USA (Wake Island)	Wake	DPS4D	19.29	166.65

2.2 Radio occultation data

The RO dataset (courtesy of Christiana Arras, GFZ Potsdam) comprises all occultations from 2020-2023 and includes tangent-point latitude/longitude, the detected sporadic-E altitude (hRO), the L1 amplitude scintillation index (S4) and a binary isSporadicE flag. The database was processed following the method of Arras and Wickert (2018), where L1 SNR profiles were normalized, L2 data were excluded due to noise, and a 2.0 km sliding-window running standard deviation of the normalized L1 SNR was applied to identify Es signatures above 50 km. A profile was flagged as sporadic E (isSporadicE = 1) when the SNR standard deviation exceeded 0.2 and the enhanced values were confined within a vertical interval of less than 10 km. The Es height (hRO) was defined as the sampling point with the maximum SNR deviation. Only profiles satisfying the isSporadicE = 1 criterion were retained for analysis. The S4 index, defined as the root-mean-square of fractional amplitude fluctuations in the 50 Hz GPS L1 signal caused by ionospheric irregularities, was used as a proxy for Es intensity; higher S4 values indicate stronger electron density gradients within or near the Es layer.

2.3 RO-Digisonde Collocation, Parameter comparisons and statistical analysis

The analysis focused on two primary parameters: (1) Es layer altitude, defined as Digisonde virtual height (hEs) versus RO-derived geometric altitude (hRO), and (2) an intensity proxy based on the fbEs and the RO amplitude scintillation index (S4). The blanketing frequency represents the highest radio frequency at which an Es layer fully obscures reflections from higher ionospheric regions and is widely regarded as a robust indicator of Es density and blanketing strength, particularly for intense or structured layers (Arras et al., 2022; Haldoupis, 2011; Sobhkhiz-Miandehi et al., 2021; Yu et al., 2023). Compared with the traditional critical frequency (foEs), fbEs provides a more direct representation of strong blanketing layers and is therefore well suited for comparison with RO-derived scintillation metrics that reflect small-scale plasma structuring (Carmona et al., 2022; Resende et al., 2018). For the analysis, only events with S4 > 0.2 were retained to isolate moderate-to-strong scintillation associated with plasma structuring and to reduce contamination from weak fluctuations or measurement noise (Brahmanandam et al., 2012; Forte and

Radicella, 2002; Van Dierendonck et al., 1993; Yeh and Liu, 1982; Yu et al., 2020). The analysis period was restricted to 2020-2023, corresponding to the stable early operational phase of COSMIC-2. RO profiles were first time-tagged using year, day-of-year, hour, and minute information and converted to a unified datetime format. The dataset was temporally ordered and restricted to parameters relevant to Es detection, including latitude, longitude, altitude, S4, and Es occurrence flags.

Profiles identified as Es events were extracted to form the working RO dataset. Spatial collocation with Digisonde observations was carried out using the RO tangent point at E-region altitudes, which represents the effective horizontal location of the satellite measurement. For each COSMIC-2 occultation, the tangent point is defined as the geographic position (latitude, longitude, and altitude) of the minimum ray-path height of the GNSS signal at a given occultation level, corresponding to the point of closest approach of the signal path to the Earth (Foelsche et al., 2010). In this study, the tangent point at the E-region altitude relevant to sporadic-E occurrence was used for RO-Digisonde collocation, and the horizontal distance between this point and the fixed Digisonde station location served as the spatial matching criterion. Each RO tangent point was assigned to the nearest Digisonde station within a fixed geographic window of $\pm 2°$ in both latitude and longitude. Profiles falling within this spatial tolerance were treated as coincident observations, yielding a consistent matched dataset suitable for statistical comparison. Temporal matching was enforced using a ± 10-minute collocation window between RO profiles and Digisonde soundings. The suitability of this temporal threshold, together with the adopted spatial criterion, was evaluated by analysing the distributions of absolute time differences (Δt) and horizontal separations (Δr) between paired observations. These station-wise distributions are summarised in Fig. 2, which illustrates the spread, median, and interquartile range of both temporal and spatial co-location differences across the network. Approximately 95% of all matched pairs occurred within a 0-5-minute interval, confirming strong temporal coincidence while maintaining sufficient sample size for statistical analysis. The absolute horizontal separation between RO tangent points and Digisonde stations ranged from near-coincident cases (<10 km) to several hundred kilometres, with the majority of matches clustered at moderate distances (~100-250 km). We note, however, that different choices of the time and/or distance thresholds could alter the number of matched RO-Digisonde pairs. No additional sensitivity test was carried out for alternative spatial or temporal windows; consequently, the reported statistics should be interpreted as conditional on the adopted $\pm 2°$ and ± 10 min criteria.

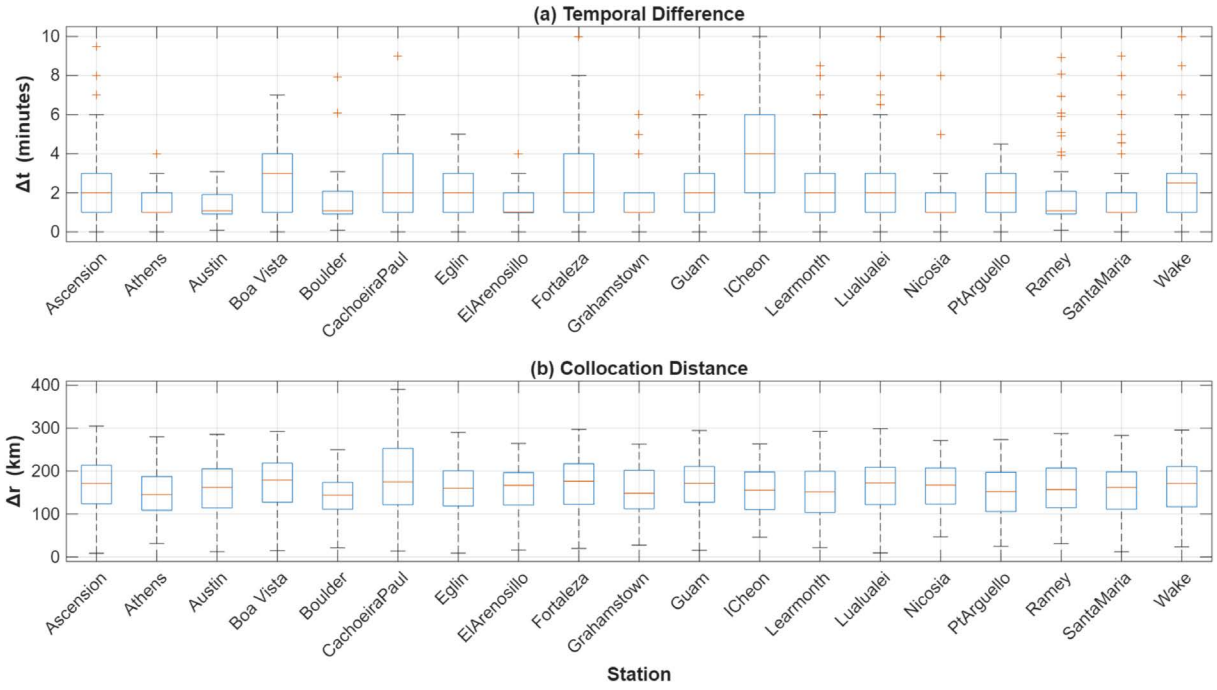

Figure 2. Station-wise distribution of co-location differences between COSMIC-2 radio occultation and Digisonde observations: (a) temporal separation, Δt (min), and (b) spatial separation, Δr (km). For each station, the box indicates the interquartile range with the median shown by the horizontal line, and the whiskers represent the data spread.

To quantify the impact of successive filtering steps on the analysed dataset, Table 2 summarises the number of RO-Digisonde matched profiles retained at each stage of data selection for all stations. The table reports (i) the total number of initially collocated profiles prior to filtering, (ii) the subset satisfying the RO sporadic-E detection flag (isSporadicE = 1), and (iii) the final subset remaining after imposing the scintillation threshold S4 > 0.2.

Table 2. Data filtering and retention statistics for RO-Digisonde matched profiles.

Station	Location	before_filter	after_isSporE = 1	after_S4 > 0.2	Matched_Profiles	pct_matched_used
AS00Q	Ascension Island	5145	1185	596	465	78.02
AT138	Athens	2078	468	136	79	58.09
AU930	Austin, TX	3924	875	371	202	54.45
BC840	Boulder, CO	2432	456	108	93	86.11
BVJ03	Boa Vista	4605	988	487	271	55.65
CAJ2M	Cachoeira Paulista	4787	897	372	320	86.02
EA036	El Arenosillo	2544	630	243	203	83.54
EI764	Eglin AFB, FL	3768	809	358	245	68.44
FZA0M	Fortaleza	4607	1162	538	473	87.92
GR13L	Grahamstown	4445	419	156	114	73.08
GU513	Guam	4709	1277	673	509	75.63
IC437	I-Cheon	3062	800	371	113	30.46
LL721	Lualualei	5048	1403	581	503	86.57
LM42B	Learmonth	4804	1305	574	265	46.17
NI135	Nicosia	2547	415	163	130	79.75
PA836	Point Arguello, CA	3218	721	284	238	83.80
PRJ18	Ramey, PR	5011	1347	714	207	28.99
SMK29	Santa Maria	3777	707	279	214	76.70
WA619	Wake	5132	1245	649	356	54.85

The column *pct_matched_used* indicates the percentage of collocated profiles retained after both filtering steps relative to the Es-detected population and available Digisonde profiles. The statistics demonstrate that the intensity analysis represents a progressively filtered subset of the available coincidences, with retention fractions varying substantially between stations (≈29-88%). This variability reflects both regional differences in scintillation occurrence and the requirement that RO measurements simultaneously detect sporadic-E and exhibit measurable amplitude scintillation. Consequently, *pct_matched_used* reflects not only the impact of the filtering criteria but

also differences in the temporal availability and successful collocation of ground-based Digisonde observations across stations. Data gaps and uneven operational coverage of individual Digisondes therefore contribute to the effective sample size. Accordingly, the fbEs-S4 comparison presented in this study characterises relationships within RO-detected and scintillating Es events supported by available ground observations rather than the full population of possible RO-Digisonde coincidences.

To mitigate the influence of storm-time electrodynamic processes on the sporadic-E diagnostics, geomagnetically disturbed days were excluded from the analysis. Planetary geomagnetic indices were taken from the GFZ Potsdam Kp-Ap product, which provides eight 3-hourly Kp estimates and a corresponding daily Ap value and is widely used for characterizing global geomagnetic activity (Yamazaki et al., 2022; Yamauchi et al., 2025). For each day, the eight 3-hourly Kp values were averaged to obtain a daily mean Kp, while the reported daily Ap index served as the primary disturbance metric, consistent with common practice in ionospheric and space-weather studies that separate quiet and disturbed conditions using planetary indices (Yamazaki et al., 2022; Ber'enyi et al., 2017). Following thresholds frequently adopted in ionospheric climatological work, days with $Ap > 20$ were classified as geomagnetically disturbed and removed from the dataset, whereas days with $Ap < 7$ were treated as geomagnetically quiet (Yamazaki et al., 2022). Only non-disturbed days ($Ap \leq 20$) were retained for constructing the RO-Digisonde collocations and for all subsequent statistical analyses. This screening step is motivated by numerous observational and modeling studies showing that prompt-penetration electric fields, disturbance dynamo electric fields, auroral energy input, and enhanced particle precipitation during storms strongly modify E-region structure, Es occurrence/intensity, and associated scintillation and irregularity signatures (Resende et al., 2021; Tahir et al., 2024; Resende et al., 2022; Imtiaz et al., 2024; Moro et al., 2017). By restricting to non-disturbed days, the derived relationships between Es peak altitude, intensity diagnostics, and RO scintillation are expected to represent the background Es climatology rather than transient storm-time perturbations.

To quantify the agreement between sporadic-E characteristics derived from radio occultation (RO) and coincident Digisonde (DIGI) measurements, a set of complementary statistical metrics was employed to characterise both the strength of association and the level of discrepancy between the two techniques. For each station, the sample size (N) denotes the total number of valid RO-DIGI measurement pairs retained after all spatial, temporal, and quality-control filters. For the Es layer altitude comparison, involving the Digisonde virtual height (h′Es) and the RO-derived geometric altitude (hRO), the Pearson correlation coefficient (R) was used to quantify the degree of linear association between the two height estimates. In addition, the root-mean-square error (RMSE) was computed to measure the absolute magnitude of the differences between RO and Digisonde heights and to provide a physically interpretable estimate of typical vertical disagreement. The corresponding mathematical expressions are provided for completeness. For the Es intensity comparison, based on the fbEs and the RO amplitude scintillation index (S4), direct error-based metrics are not appropriate because the two parameters have different physical units and represent distinct aspects of Es intensity. Accordingly, the comparison focuses on statistical association rather than absolute differences. The Pearson correlation coefficient (R) was computed to assess linear dependence, while Spearman's rank correlation coefficient (ρ) and Kendall's rank correlation coefficient (τ) were used to evaluate monotonic relationships that are robust to nonlinearity and outliers. The p-value associated with each correlation metric was calculated to assess statistical significance.

3. Results

This section presents the comparison of sporadic E (Es) characteristics derived from radio occultation and Digisonde observations, focusing on peak altitude and intensity. Peak altitude is evaluated using hRO and hEs, and intensity is assessed through the S4 scintillation index and the fbEs.

3.1 Es Layer Altitudes from RO and Digisonde

Station-wise comparisons of COSMIC-2 radio occultation-derived sporadic-E peak heights (hEs_RO) and coincident Digisonde measurements (hEs_DIGI) across 19 stations spanning equatorial, low, mid, and low-to-mid geomagnetic latitudes reveal a generally positive association between the two datasets, although the strength of the relationship and the degree of scatter about the one-to-one line vary substantially between sites. Pearson correlation

coefficients range from 0.22 to 0.66, indicating weak to moderately strong linear agreement across the station network. The detailed station-level relationships are illustrated in Fig. 3, while Fig. 4 summarises the corresponding RMSE, Pearson correlation, boxplot, and mean bias statistics describing the level of agreement between the two measurement techniques across stations.

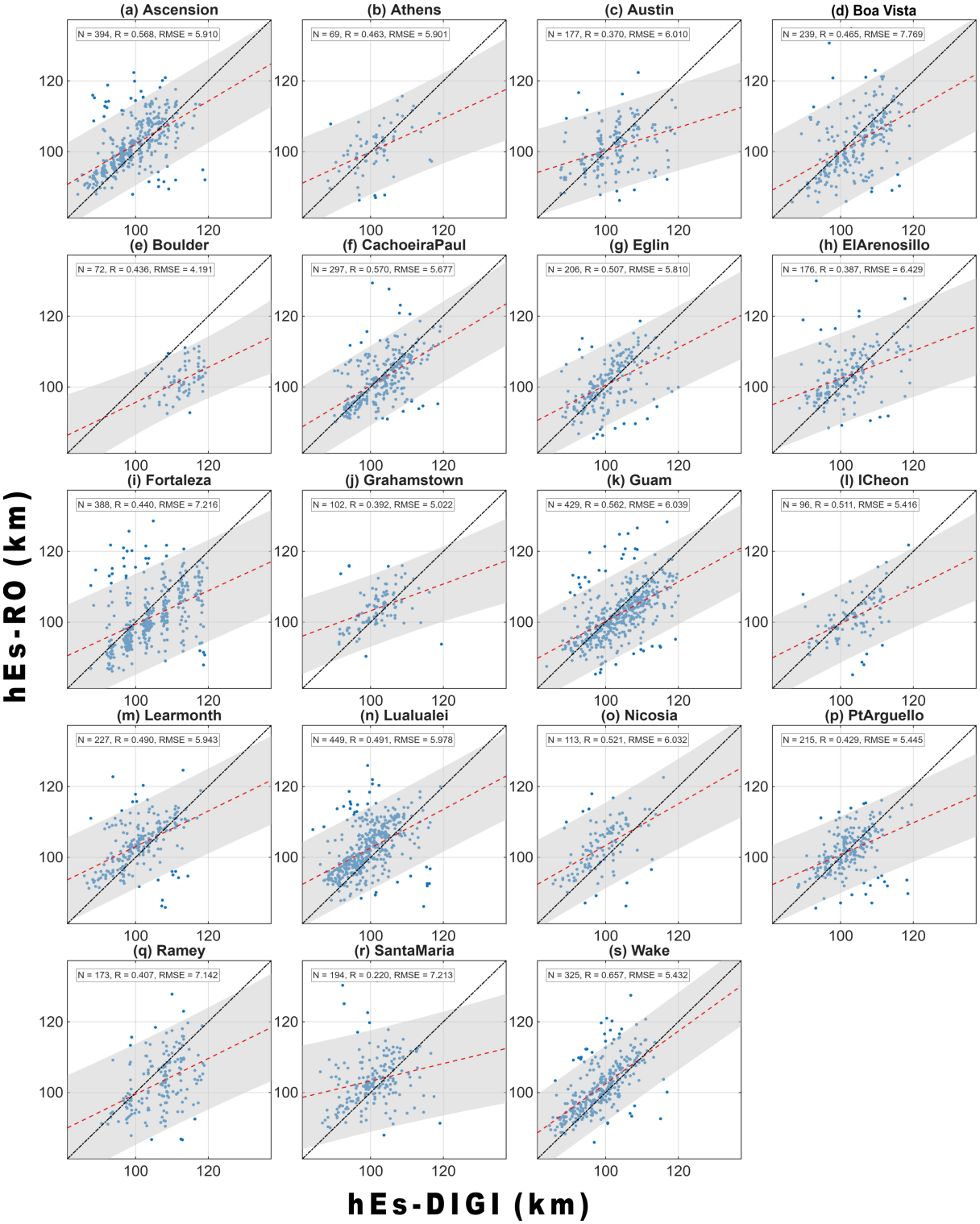

Figure 3. Scatter plots of RO-derived sporadic-E peak height (hEs_RO) versus Digisonde-measured peak height (hEs_DIGI) for all stations. Each panel (a-s) corresponds to one station. Blue points represent paired measurements, the black solid line denotes the 1:1 reference line, and the red dashed line shows the linear regression fit; grey shading indicates the 95% confidence band of the regression.

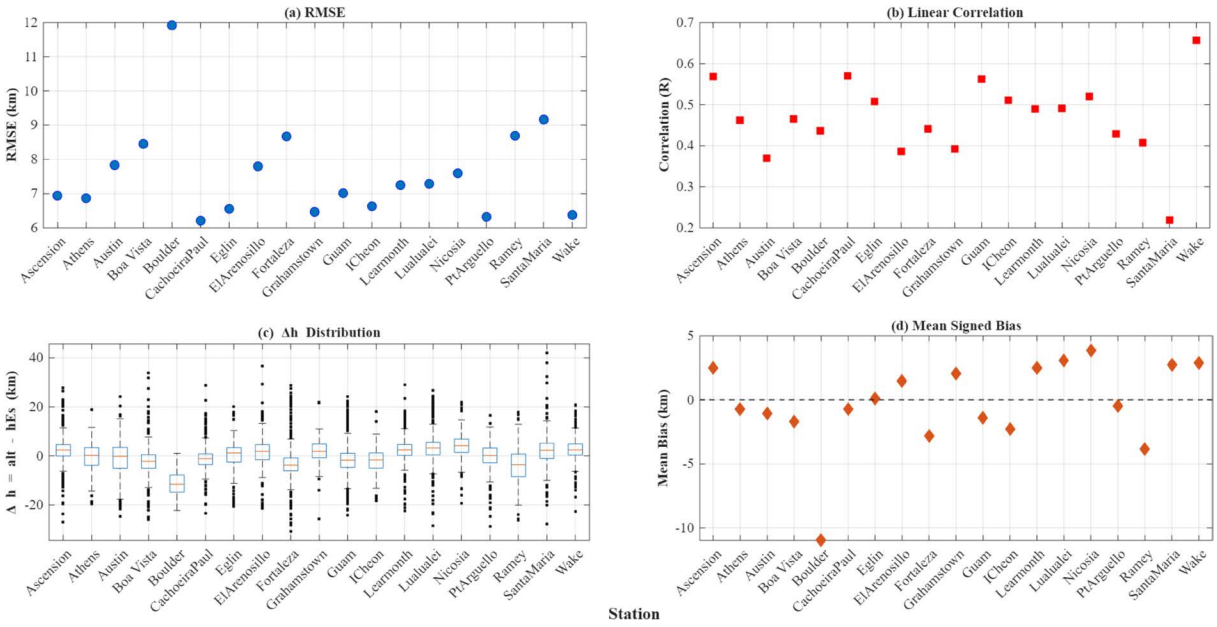

Figure 4. Summary statistics of sporadic-E peak altitude comparison between RO and Digisonde across stations. Panel (a) root-mean-square error (RMSE) of RO-derived peak altitude (alt) relative to Digisonde virtual height (h′Es); panel (b) Pearson linear correlation coefficient (R) between alt and h′Es at each station; panel (c) station-wise boxplots of the signed altitude difference (Δh = alt – h′Es), illustrating median bias, interquartile range, and outliers; and panel (d) mean signed bias (Δh) with the horizontal dashed line indicating zero bias.

The strongest agreement is observed at Wake, which exhibits the highest correlation (R = 0.66) based on 325 coincident observations. Other stations with relatively strong correlations include Cachoeira Paulista (R = 0.57, N = 297), Ascension (R = 0.57, N = 394) and Guam (R = 0.56, N = 429). These stations also benefit from comparatively large sample sizes, enhancing the statistical robustness of the derived correlations. In contrast, Santa Maria shows the weakest agreement, with a correlation coefficient of R = 0.22 based on 194 collocations, indicating substantial dispersion between RO- and digisonde-derived Es peak heights at this location. Several additional stations, including Boa Vista, Fortaleza and Ramey, also display reduced correlations relative to the group of stations with the highest correlations.

Root-mean-square error values for the paired measurements span approximately 4.2 to 7.8 km, with a multi-station mean close to 6 km. The smallest RMSE is obtained at Boulder (4.19 km), while the largest RMSE values are recorded at Boa Vista (7.77 km), Fortaleza (7.22 km), Santa Maria (7.21 km) and Ramey (7.14 km). At the majority of stations, RMSE values lie between about 5 and 6 km, placing them within a moderate agreement range in terms of absolute height differences. Notably, the correspondence between correlation strength and RMSE is not one-to-one. For example, Boulder exhibits relatively small absolute height differences despite only moderate correlation (R = 0.44), indicating that low RMSE does not necessarily imply a strong linear relationship.

When the results are considered by latitude, two distinct patterns emerge. Low-latitude and equatorial stations, including Wake, Ascension, Guam and Cachoeira Paulista, generally exhibit higher correlations, typically in the range of approximately 0.50 to 0.66, together with lower RMSE values of about 5 to 6 km. In contrast, other equatorial and low-latitude stations such as Boa Vista, Fortaleza and Ramey are characterised by weaker correlations, ranging from approximately 0.22 to 0.46, and larger RMSE values approaching 7 to 8 km. Hence, COSMIC-2 radio occultation measurements reproduce the broad statistical distribution of Digisonde sporadic-E peak heights across the global network, although individual coincident estimates frequently differ by several kilometres and the level of agreement exhibits strong site-to-site variability.

3.2 Intensity Comparison: Scintillation Index vs. blanketing frequency of the Es layer

The relationship between RO-derived S4 and Digisonde fbEs is consistently positive across all stations considered but generally weak to moderate in magnitude, with pronounced geographic variability in both strength and statistical

significance, as illustrated by the station-wise scatter distributions in Fig. 5 and quantified by the statistical metrics shown in Fig. 6. Pearson correlation coefficients range from 0.019 at Athens to 0.358 at Boa Vista, indicating that the strongest linear coupling is observed at Boa Vista (R = 0.358), Boulder (R = 0.349), and Lualualei (R = 0.305), whereas

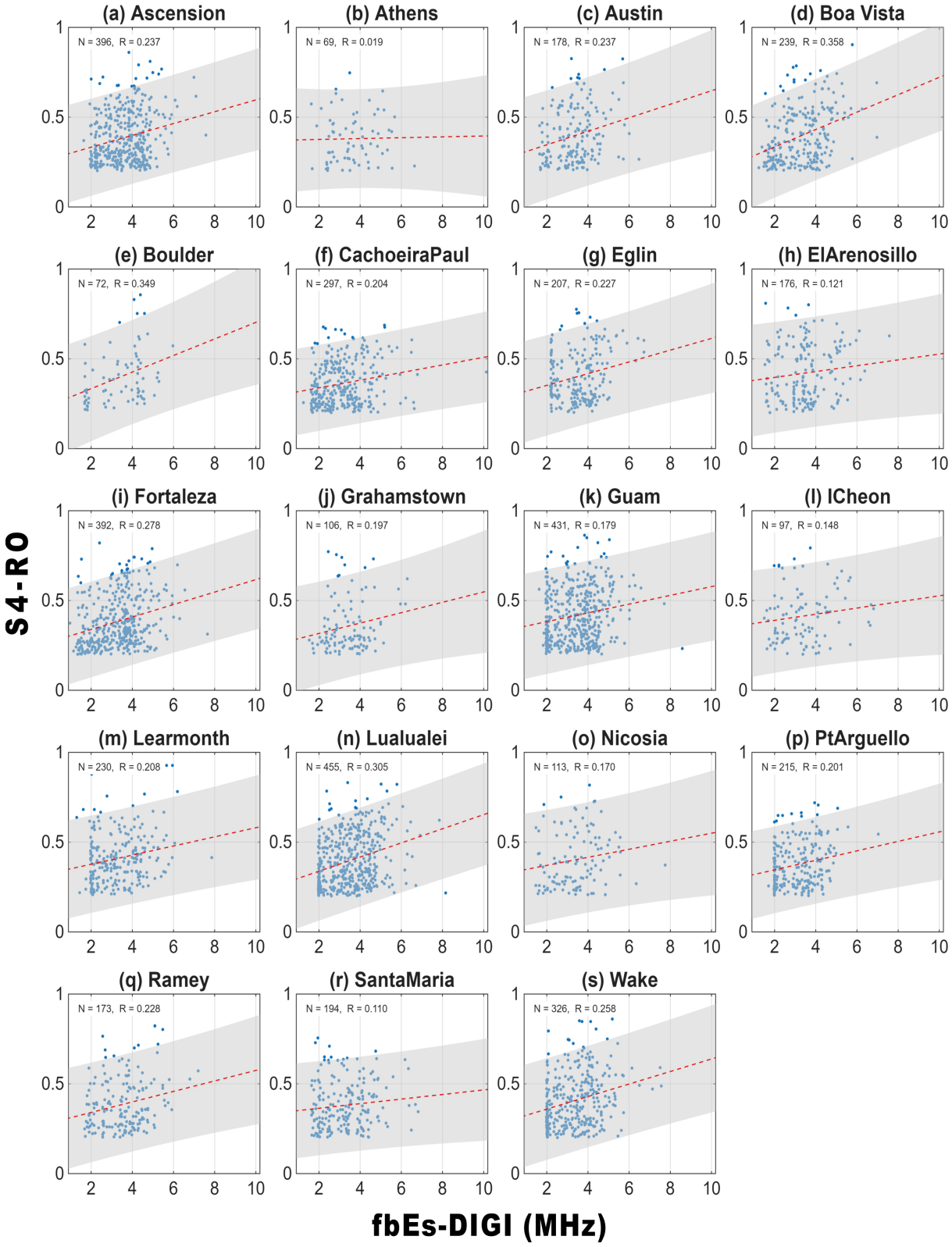

Figure 5. Scatter plots of RO-S4 versus Digisonde fbEs for all stations. Each panel (a-s) corresponds to one station. Blue points represent paired measurements, the red dashed line shows the linear regression fit, and grey shading indicates the 95% confidence band of the regression.

stations such as Athens (R = 0.019) and Santa Maria (R = 0.110) exhibit negligible linear association between S4 and fbEs. This behaviour is reflected in the corresponding scatter plots (Fig. 5), where stations with higher correlation coefficients display a discernible positive trend and narrower confidence envelopes around the regression fit, while low-correlation stations show diffuse point clouds with little organised structure. Non-parametric measures further corroborate this pattern: Spearman's rank correlation coefficient reaches a maximum of 0.347 and Kendall's τ peaks at 0.235 for Boa Vista, whereas the lowest values occur at Athens and El Arenosillo, confirming that where linear correlations are weak, the underlying monotonic ordering between S4 and fbEs is also limited.

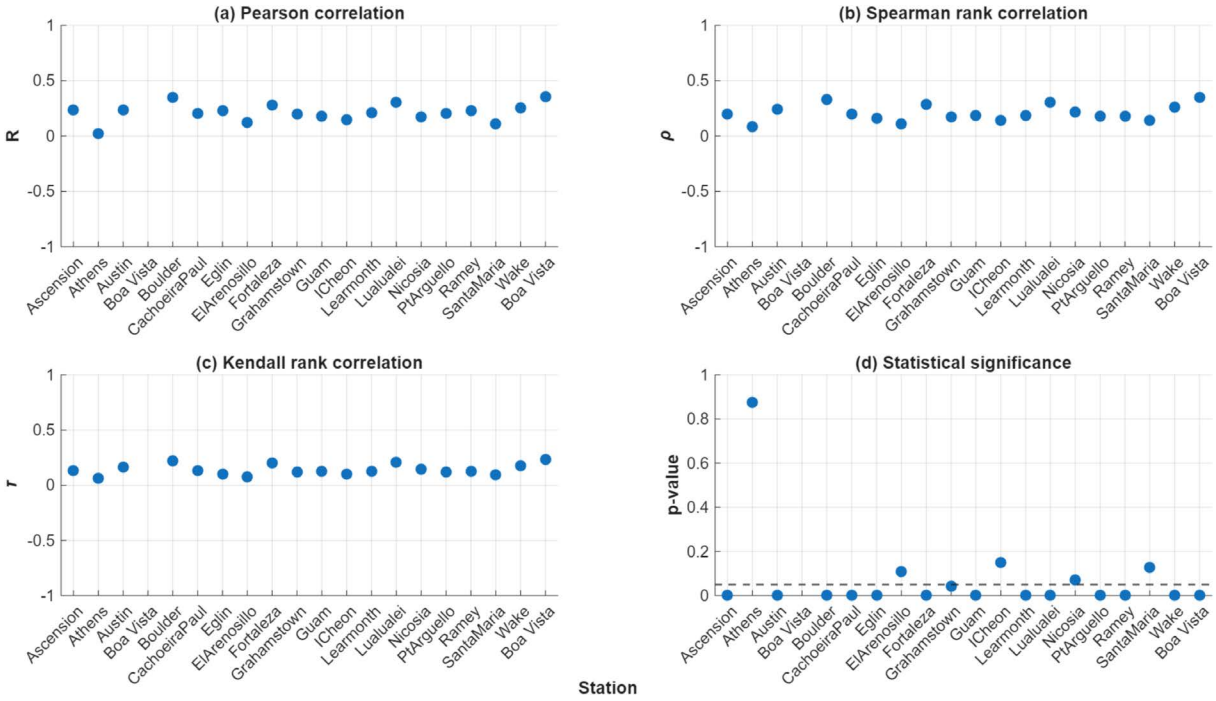

Figure 6. Station-wise statistical measures quantifying the relationship between RO-derived S4 and Digisonde fbEs.

Statistical significance is achieved at 14 of the 19 stations, with $p < 0.01$ at a large subset including Ascension, Boa Vista, Boulder, Lualualei, Fortaleza, and Wake, indicating that in these regions higher fbEs is reliably associated with enhanced scintillation as measured by S4. In contrast, Athens ($p = 0.8745$), El Arenosillo ($p = 0.1101$), I-Cheon ($p = 0.1492$), Nicosia ($p = 0.0717$), and Santa Maria ($p = 0.1262$) do not exhibit statistically significant relationships, and their scatter plots in Fig. 5 are characterised by diffuse scatter and nearly flat regression lines, suggesting that at these mid-latitude and low-latitude stations, fbEs provides only a weak indication of S4 variability. Even where the relationship is strongest, the modest magnitudes ($R \leq 0.358$) imply that fbEs alone explains no more than about 13% of S4 variance, underscoring the role of additional geophysical factors in controlling scintillation levels.

A pronounced latitudinal dependence emerges. Equatorial stations (Ascension, Boa Vista, Fortaleza) display the most coherent and statistically robust relationships, with Boa Vista exhibiting $R = 0.358$, $\rho = 0.347$, $\tau = 0.235$ and $p \approx 1.23 \times 10^{-8}$, while Fortaleza ($R = 0.278$; $\rho = 0.288$; $\tau = 0.200$; $p \approx 2.28 \times 10^{-8}$) and Ascension ($R = 0.237$; $\rho = 0.198$; $\tau = 0.134$; $p \approx 1.76 \times 10^{-6}$) show slightly weaker but still highly significant monotonic behaviour. The tighter clustering and clear upward trends in the equatorial stations of Fig. 5 thus reflect comparatively consistent coupling between Es blanketing strength and RO scintillation in low-latitude ionospheric conditions. Low-latitude stations show mixed but still predominantly significant behaviour: Lualualei yields $R = 0.305$, $\rho = 0.308$, $\tau = 0.209$ with $p \approx 2.97 \times 10^{-11}$, while Wake and Ramey maintain weaker yet clear positive trends, and Guam and Learmonth exhibit statistically significant but reduced correlation magnitudes ($R \approx 0.18$-0.21). Santa Maria, situated at the edge of the low-latitude range, is the only station that does not exhibit a statistically significant relationship ($R = 0.110$; $p \approx 0.126$), as reflected by the diffuse scatter of fbEs-S4 pairs.

Mid-latitude stations exhibit the widest spread in behaviour, from the relatively strong and significant coupling at Boulder ($R = 0.349$; $\rho = 0.327$; $\tau = 0.224$; $p \approx 0.0026$) to the virtually negligible, non-significant relationship at

Athens ($R = 0.019$; $p = 0.8745$) and the weak, marginal results at El Arenosillo, I-Cheon, and Nicosia. This heterogeneity indicates that at mid-latitudes the fbEs-S4 linkage is more sensitive to station-specific conditions, and that sporadic-E blanketing frequency alone is often insufficient to characterise scintillation. When viewed hemispherically, Northern and Southern stations collectively span similar ranges of R, from very weak at Athens ($R = 0.019$) to moderately strong at Boulder and Lualualei ($R \approx 0.30$-0.35), with Southern stations such as Ascension, Fortaleza, Cachoeira Paulista, and Learmonth mostly showing weak-to-moderate but significant correlations and Santa Maria providing the weakest southern result ($R = 0.110$; $p \approx 0.126$). Consequently, no systematic hemispheric dominance is evident; instead, correlation strength is more clearly organized by latitudinal dependence.

The integration of quantitative metrics (Fig. 6) with the scatter plots in Fig. 5 reveals a consistent correspondence between statistical indicators and visual patterns: stations with higher Pearson and rank-based coefficients, such as Boa Vista, Boulder, Lualualei, and Fortaleza, display well-defined upward trends and relatively narrow confidence bands, whereas low- or non-significant stations like Athens, Santa Maria, El Arenosillo, and I-Cheon are characterised by broadly dispersed points and shallow regression slopes. The positive sign of all three correlation measures at every station and the predominance of statistically significant results indicate that S4 scintillation amplitudes derived from radio occultation systematically increase with Digisonde fbEs, but that the strength and reliability of this coupling are strongly modulated by latitude, local ionospheric conditions, and residual effects associated with sampling density and collocation uncertainty.

4. Discussion

The level of agreement between RO-derived sporadic-E peak heights and Digisonde estimates reflects a combination of methodological differences, sampling geometry, and genuine geophysical variability that is characteristic of RO-ionosonde intercomparisons. A primary source of discrepancy arises from differences in height definition. COSMIC-2 radio occultation retrieves geometric altitudes associated with refractivity or electron density perturbations along slanted ray paths, whereas Digisonde measurements provide virtual heights inferred from ionogram traces. Virtual heights are known to overestimate true Es altitudes depending on background ionisation, local time, and E-region plasma conditions, introducing station-dependent biases that contribute to the observed spread in correlation and RMSE values (Arras and Wickert, 2017; Gan et al., 2022; Haldoupis et al., 2024; Yan et al., 2025; Zeng et al., 2019). The magnitude of these discrepancies is consistent with earlier studies based on FORMOSAT-3/COSMIC and CHAMP observations, indicating that the observed mismatch reflects inherent methodological and physical limitations rather than anomalous behaviour at specific sites (Arras et al., 2008; Gooch et al., 2020; Resende et al., 2018).

Fundamental constraints of radio occultation retrievals further affect peak height determination. The finite vertical resolution and smoothing inherent to RO processing tend to broaden sporadic-E layers that are often only a few kilometres thick, which can shift the apparent altitude of the retrieved peak relative to the sharper structures resolved in ionograms. These effects are amplified during events with multiple or vertically structured Es layers, increasing scatter in the hEs_RO-hEs_DIGI relationship (Ellis et al., 2024; Liu et al., 2024; Qiu et al., 2021; Xu et al., 2022; Yu et al., 2023). In addition, imperfect spatial and temporal collocation between RO tangent points and fixed Digisonde locations introduces further variability. Even within standard coincidence windows, horizontal separations of tens to hundreds of kilometres and temporal offsets of several minutes allow real spatial gradients and rapid temporal evolution of Es layers to decorrelate paired observations, a limitation that is particularly important given the localised and transient nature of sporadic-E structures (Gan et al., 2022; Gooch et al., 2020; Resende et al., 2018; Shaver et al., 2023).

Improved correspondence is generally observed in regions where Es layers are horizontally extensive and relatively uniform, conditions under which both slanted RO paths and vertical Digisonde soundings sample similar structures (Arras et al., 2009; Carmona et al., 2022). Oceanic and equatorial environments influenced by smoother tidal forcing and reduced gravity-wave activity tend to favour coherent layer formation and more consistent height estimates (Arras et al., 2022; Chu et al., 2014). By contrast, regions characterised by strong tidal variability, gravity-wave modulation, and complex electrodynamic forcing frequently produce patchy and short-lived Es layers that are not equivalently sampled by the two techniques, leading to reduced agreement similar to that reported over South America and other dynamically complex regions (Resende et al., 2018; Sobhkhiz-Miandehi et al., 2023). Differences in dominant formation mechanisms further contribute to this variability, as mid-latitude wind-shear-driven Es layers

tend to exhibit greater vertical coherence than low-latitude electrodynamically driven layers, which are often more irregular and rapidly evolving (Qiu et al., 2021; Sobhkhiz-Miandehi et al., 2021; Yu et al., 2023).

A similar interpretation applies to the relationship between COSMIC-2 amplitude scintillation and Digisonde blanketing frequency. The S4-fbEs comparison reveals a consistently positive but generally modest association between Es layer intensity and L-band amplitude scintillation, with correlation magnitudes that vary substantially between stations. Stronger and statistically significant relationships are observed at some equatorial and low-latitude sites, whereas weak or insignificant associations occur at several mid-latitude locations. This spatial heterogeneity reflects both physical and observational factors and frames the interpretation of the S4-fbEs coupling. A fundamental limitation is that fbEs and S4 characterise different physical aspects of sporadic-E. The blanketing frequency represents the layer's bulk blanketing capability and thus its integrated metal-ion content, whereas S4 is controlled by the presence of sharp electron-density gradients and small-scale irregularities at Fresnel and sub-Fresnel scales. Observational and modelling studies demonstrate that multiple combinations of layer thickness, peak density, and horizontal extent can produce similar S4 values, and that S4 tends to saturate for strong layers such that further increases in bulk density do not translate into proportionally larger scintillation amplitudes (Emmons et al., 2022; Yu et al., 2020). As a result, high fbEs does not necessarily imply strong S4, while moderate fbEs can coincide with intense scintillation when fine-scale structuring is present.

Instrumental and parameter-definition effects further weaken simple statistical relationships. Standard Digisonde parameters such as fbEs can be influenced by background E-region plasma, particularly under daytime conditions, obscuring the metal-ion signal most relevant for scintillation generation (Haldoupis et al., 2023, 2025). Recent proposals to derive metal-ion-corrected indices, such as fbμEs, aim to remove ambient electron density contributions and provide closer proxies for the structures that control S4, and their use is expected to strengthen RO-ionosonde correspondence, especially during high solar conditions (Haldoupis et al., 2023, 2025). At the same time, RO-derived intensity proxies are subject to slant-path integration and geometric smoothing, which can attenuate sharp, localised irregularities that would produce large S4 in vertical or near-nadir observations (Emmons et al., 2022; Yue et al., 2015). Differences in sampling geometry introduce additional decorrelation. Digisonde soundings represent near-vertical measurements at fixed locations, whereas COSMIC-2 occultations sample extended slant paths whose tangent points may be displaced by hundreds of kilometres. Given the spatial intermittency and rapid evolution of Es layers, such mismatches inevitably reduce linear association metrics (Merriman et al., 2021; Niu et al., 2019; Yu et al., 2020). The persistence of statistically significant positive correlations at many stations nevertheless indicates that the underlying physical linkage between bulk Es intensity and scintillation is robust enough to be detectable despite these limitations (Emmons et al., 2022; Niu et al., 2019; Yu et al., 2020).

Geographic and climatological factors control how efficiently bulk Es content is converted into small-scale irregularities and thus into scintillation. Wind-shear-driven metallic-ion convergence, tidal forcing, geomagnetic latitude, and background ionisation establish systematic spatial and seasonal patterns in Es morphology. Where layers are climatologically coherent and frequently blanketing, the mapping from fbEs to S4 is more stable and correlations are higher (Niu et al., 2019; Niu and Fang, 2023). In contrast, regions characterised by intermittent or morphologically smooth Es tend to exhibit weaker scintillation responses for a given fbEs, producing the low correlations observed at some mid-latitude sites (Merriman et al., 2021; Resende et al., 2018). Finally, nonlinearities in scintillation generation impose fundamental limits on linear correlation metrics. Both simulations and observations show that S4 increases with irregularity strength only up to moderate intensities, beyond which saturation and insensitivity to further increases in bulk layer strength reduce the explanatory power of a single scalar index such as fbEs (Emmons et al., 2022; Yu et al., 2020). Together with the non-unique relationship between layer structure and resulting scintillation amplitude, these factors mean that bulk intensity parameters can account for only a limited portion of the observed S4 variability, even when measurements are ideally collocated.

5. Conclusions

This study presents a station-wise evaluation of sporadic-E altitude and intensity derived from coincident COSMIC-2 radio occultation and Digisonde measurements across 19 globally distributed stations. RO-derived Es peak heights reproduce the broad statistical behaviour of Digisonde virtual heights, with Pearson correlations ranging from 0.22 to 0.66 and typical RMSE values of approximately 5-6 km. The magnitude and structure of these differences are consistent with established RO-ionosonde comparisons and are attributable primarily to disparities in sampling

geometry, vertical resolution, and the fundamental distinction between geometric (RO) and virtual (ionosonde) height definitions, rather than site-specific anomalies. The intensity analysis demonstrates a uniformly positive but modest association between RO L-band amplitude scintillation and Digisonde blanketing frequency, with statistically significant correlations at most stations and comparatively stronger agreement at equatorial and low-latitude locations. The limited proportion of S4 variance explained by fbEs reflects the differing physical sensitivities of the parameters: fbEs quantifies bulk blanketing strength, whereas S4 responds to small-scale electron density gradients and irregularity spectra along the occultation ray path, and is further influenced by nonlinear saturation and collocation uncertainty. The filtering statistics summarised in Table 2 indicate that the analysis applies to a conditioned subset of RO-detected and scintillating events, and thus represents a comparative benchmarking assessment rather than a complete sampling of global sporadic-E occurrence. The findings should be viewed as a basis for future refinement of sporadic-E climatologies and empirical models, and not as evidence of an implemented data-assimilation capability.

Data availability statement. The Digisonde ionograms were obtained from the Lowell GIRO Data Center, University of Massachusetts Lowell (https://ulcar.uml.edu). The radio occultation data were provided by GFZ Potsdam and are available upon request through the GFZ Ionosphere Group Data Services (https://dataservices.gfz-potsdam.de).

Acknowledgements. The authors thank Dr. Christina Arras (GFZ Potsdam) for providing the processed sporadic E database derived from radio occultation data. Digisonde ionograms were obtained from the Digital Ionogram Database (DIDBase) of the Lowell GIRO Data Center, University of Massachusetts Lowell.

References

Arras, C. and J. Wickert (2017). Estimation of ionospheric sporadic E intensities from GPS radio occultation measurements, J. Atmos. Sol.-Terr. Phys., 171, 60-63, doi:10.1016/j.jastp.2017.08.006.

Arras, C., C. Jacobi and J. Wickert (2009). Semidiurnal tidal signature in sporadic E occurrence rates derived from GPS radio occultation measurements at higher midlatitudes, Ann. Geophys., 27, 2555-2563, doi:10.5194/angeo-27-2555-2009.

Arras, C., C. Jacobi, J. Wickert, S. Heise and T. Schmidt (2010). Sporadic E signatures revealed from multi-satellite radio occultation measurements, Adv. Radio Sci., 8, 225-230, doi:10.5194/ars-8-225-2010.

Arras, C., J. Wickert, G. Beyerle, S. Heise, T. Schmidt and C. Jacobi (2008). A global climatology of ionospheric irregularities derived from GPS radio occultation, Geophys. Res. Lett., 35, doi:10.1029/2008GL034158.

Arras, C., L. C. A. Resende, A. Kepkar, G. Senevirathna and J. Wickert (2022). Sporadic E layer characteristics at equatorial latitudes as observed by GNSS radio occultation measurements, Earth Planets Space, 74,1, 1-15, doi:10.1186/s40623-022-01718-y.

Axford, W. I. and D. M. Cunnold (1966). The wind-shear theory of temperate zone sporadic E, Radio Sci., 1, 2, 191, doi:10.1002/rds196612191.

Berényi, K. A., V. Barta and Á. Kis (2018). Midlatitude ionospheric F2-layer response to eruptive solar events-caused geomagnetic disturbances over Hungary during the maximum of solar cycle 24: A case study, Adv. Space Res., 61, 5, 1230-1243, doi:10.1016/j.asr.2017.12.021.

Bilitza, D., M. Pezzopane, V. Truhlik, D. Altadill, B. W. Reinisch and A. Pignalberi (2022). The International Reference Ionosphere model: A review and description of an ionospheric benchmark, Rev. Geophys., 60, 4, e2022RG000792, doi:10.1029/2022RG000792.

Brahmanandam, P. S., G. Uma, J. Y. Liu, Y. H. Chu et al. (2012). Global S4 index variations observed using FORMOSAT-3/COSMIC GPS RO technique during a solar minimum year, J. Geophys. Res. Space Phys., 117, A9, A09322, doi:10.1029/2012JA017966.

Carmona, R., O. Nava, E. Dao and D. Emmons (2022). A comparison of sporadic-E occurrence rates using GPS radio occultation and ionosonde measurements, Remote Sens., 14, 581, doi:10.3390/rs14030581.

Christakis, N., C. Haldoupis, Q. Zhou and C. Meek (2009). Seasonal variability and descent of mid-latitude sporadic E layers at Arecibo, Ann. Geophys., 27, 3, 923-931, doi:10.5194/angeo-27-923-2009.

Chu, Y. H., C. Y. Wang, K. H. Wu, K. T. Chen et al. (2014). Morphology of sporadic E layer retrieved from COSMIC GPS radio occultation measurements: Wind shear theory examination, J. Geophys. Res. Space Phys., 119, 3, 2117-2136, doi:10.1002/2013JA019437.

Didebulidze, G. G. and L. Lomidze (2008). The formation of sporadic E layers by a vortical perturbation excited in a horizontal wind shear flow, Ann. Geophys., 26, 7, 1741, doi:10.5194/angeo-26-1741-2008.

Ellis, J., D. Emmons and M. Cohen (2024). Detection and classification of sporadic E using convolutional neural networks, Space Weather, 22, e2023SW003669, doi:10.1029/2023SW003669.

Emmons, D., D. Wu and N. Swarnalingam (2022). A statistical analysis of sporadic-E characteristics associated with GNSS radio occultation phase and amplitude scintillations, Atmosphere, 13, 12, 2098, doi:10.3390/atmos13122098.

Emmons, D. J., D. L. Wu, N. Swarnalingam, A. F. Ali et al. (2023). Improved models for estimating sporadic-E intensity from GNSS radio occultation measurements, Front. Astron. Space Sci., 10, 1327979, doi:10.3389/fspas.2023.1327979.

Foelsche, U., S. Syndergaard, J. Fritzer and G. Kirchengast (2011). Errors in GNSS radio occultation data: Relevance of the measurement geometry and obliquity of profiles, Atmos. Meas. Tech., 4, 189-199, doi:10.5194/amt-4-189-2011.

Forte, B. and S. M. Radicella (2002). Problems in data treatment for ionospheric scintillation measurements, Radio Sci., 37, 6, 1096, doi:10.1029/2001RS002508.

Gan, C., J. Hu, X. Luo, C. Xiong and S. Gu (2022). Sounding of sporadic E layers from China Seismo-Electromagnetic Satellite (CSES) radio occultation and comparing with ionosonde measurements, Ann. Geophys., 40,4, 463-474, doi:10.5194/angeo-40-463-2022.

Gooch, J., J. Colman, O. Nava and D. Emmons (2020). Global ionosonde and GPS radio occultation sporadic-E intensity and height comparison, J. Atmos. Sol.-Terr. Phys., 199, 105200, doi:10.1016/j.jastp.2020.105200.

Haldoupis, C. (2011). A tutorial review on sporadic E layers, in: Aeronomy of the Earth's Atmosphere and Ionosphere, IAGA Spec. Sopron Book Ser., 2, 381-394, doi:10.1007/978-94-007-0326-1_29.

Haldoupis, C. (2012). Midlatitude sporadic E: A typical paradigm of atmosphere-ionosphere coupling, Space Sci. Rev., 168, 441-461, doi:10.1007/s11214-011-9786-8.

Haldoupis, C. (2019). An improved ionosonde-based parameter to assess sporadic E layer intensities: A simple idea and an algorithm, J. Geophys. Res. Space Phys., 124, 2127-2134, doi:10.1029/2018JA026441.

Haldoupis, C., H. Haralambous and C. Meek (2024). A simplified method of true height analysis to estimate the real height of sporadic E layers, J. Geophys. Res. Space Phys., 129, e2024JA032505, doi:10.1029/2024JA032505.

Haldoupis, C., H. Haralambous and C. Meek (2025). An updated method and algorithm for computing improved ionosonde-based sporadic E layer parameters, J. Geophys. Res. Space Phys., 130, e2025JA034122, doi:10.1029/2025JA034122.

Haldoupis, C., H. Haralambous, C. Meek and J. Mathews (2023). Understanding the diurnal cycle of midlatitude sporadic E: The role of metal atoms, J. Geophys. Res. Space Phys., 128, e2023JA031336, doi:10.1029/2023JA031336.

Hodos, T. J., O. A. Nava, E. V. Dao and D. J. Emmons (2022). Global sporadic-E occurrence rate climatology using GPS radio occultation and ionosonde data, J. Geophys. Res. Space Phys., 127, 12, e2022JA030795, doi:10.1029/2022JA030795.

Igarashi, K., M. Nakamura, P. Wilkinson, J. Wu et al. (2001). Global sounding of sporadic E layers by the GPS/MET radio occultation experiment, J. Atmos. Sol.-Terr. Phys., 63, 18, 1973-1980, doi:10.1016/S1364-6826(01)00063-3.

Ikubanni, S. O. and J. O. Adeniyi (2017). Relationship between ionospheric F2-layer critical frequency, F10.7, and F10.7P around African EIA trough, Adv. Space Res., 59, 4, 1014-1022, doi:10.1016/j.asr.2016.11.013.

Imtiaz, N., T. Dugassa, A. Calabia, C. Anoruo and A. Kashcheyev (2024). Westward PPEF plays important role in the suppression of post-midnight plasma irregularities: A case study of the November 2021 geomagnetic storm, J. Geophys. Res. Space Phys., 129, e2023JA032367, doi:10.1029/2023JA032367.

Knisely, A. J. and D. J. Emmons (2023). Impacts of Kelvin-Helmholtz billow formation on GNSS radio occultation measurements of sporadic-E, Front. Astron. Space Sci., 10, doi:10.3389/fspas.2023.1280228.

Liu, H., X. Xu, J. Luo and T. Hu (2024). Using radio occultation-based electron density profiles for studying sporadic E layer spatial and temporal characteristics, Earth Planets Space, 76, 1-18, doi:10.1186/s40623-024-02038-z.

Luo, J., H. Liu and X. Xu (2021). Sporadic E morphology based on COSMIC radio occultation data and its relationship with wind shear theory, Earth Planets Space, 73, 1, 1-17, doi:10.1186/s40623-021-01550-w.

Mathews, J. D. (1998). Sporadic E: Current views and recent progress, J. Atmos. Sol.-Terr. Phys., 60, 413-435, doi:10.1016/S1364-6826(97)00043-6.

Merriman, D., O. Nava, E. Dao and D. Emmons (2021). Comparison of seasonal foEs and fbEs occurrence rates derived from global digisonde measurements, Atmosphere, 12, 12, 1558, doi:10.3390/atmos12121558.

Moro, J., L. Resende, C. Denardini, J. Xu et al. (2017). Equatorial E-region electric fields and sporadic E layer responses to the recovery phase of the November 2004 geomagnetic storm, J. Geophys. Res. Space Phys., 122, 12517-12533, doi:10.1002/2017JA024734.

Moro, J., J. Xu, J. V. Bageston, L. A. da Silva et al. (2025). Study of height-spread sporadic-E layers observed in the South American Magnetic Anomaly, Front. Astron. Space Sci., 12, 1535186, doi:10.3389/fspas.2025.1535186.

Niu, J. and H. Fang (2023). An empirical model of the sporadic E layer intensity based on COSMIC radio occultation observations, Space Weather, 21, 1, e2022SW003280, doi:10.1029/2022SW003280.

Niu, J., L. Weng, X. Meng and H. Fang (2019). Morphology of ionospheric sporadic E layer intensity based on COSMIC occultation data in the midlatitude and low-latitude regions, J. Geophys. Res. Space Phys., 124, 10716-10730, doi:10.1029/2019JA026828.

Qiu, L., T. Yu, X. Yan, Y. Sun, X. Zuo et al. (2021). Altitudinal and latitudinal variations in ionospheric sporadic-E layer obtained from FORMOSAT-3/COSMIC radio occultation, J. Geophys. Res. Space Phys., 126, e2021JA029454, doi:10.1029/2021JA029454.

Resende, L. C. A., C. Arras, I. S. Batista, C. M. Denardini et al. (2018). Study of sporadic E layers based on GPS radio occultation measurements and Digisonde data over the Brazilian region, Ann. Geophys., 36, 587-593, doi:10.5194/angeo-36-587-2018.

Resende, L., J. Shi, C. Denardini, I. Batista, G. Picanço et al. (2021). The impact of the disturbed electric field in the sporadic E (Es) layer development over Brazilian region, J. Geophys. Res. Space Phys., 126, e2020JA028598, doi:10.1029/2020JA028598.

Resende, L., Y. Zhu, C. Arras, C. Denardini et al. (2022). Analysis of the sporadic-E layer behavior in different American stations during the days around the September 2017 geomagnetic storm, Atmosphere, 13, 1714, doi:10.3390/atmos13101714.

Schreiner, W. S., J. P. Weiss, R. A. Anthes, J. Braun et al. (2020). COSMIC-2 radio occultation constellation: First results, Geophys. Res. Lett., 47, e2019GL086841, doi:10.1029/2019GL086841.

Shaver, D., D. Wu, N. Swarnalingam, A. Franz et al. (2023). Comparison of a bottom-up GNSS radio occultation method to measure D- and E-region electron densities with ionosondes and FIRI, Remote Sens., 15, 4363, doi:10.3390/rs15184363.

Sobhkhiz-Miandehi, S., Y. Yamazaki, C. Arras and D. Themens (2023). A comparison of FORMOSAT-3/COSMIC radio occultation and ionosonde measurements in sporadic E detection over mid- and low-latitude regions, Front. Astron. Space Sci., 10, doi:10.3389/fspas.2023.1198071.

Sobhkhiz-Miandehi, S., Y. Yamazaki, C. Arras, Y. Miyoshi and H. Shinagawa (2021). Comparison of the tidal signatures in sporadic E and vertical ion convergence rate, Earth Planets Space, 74, 1-13, doi:10.1186/s40623-022-01637-y.

Swarnalingam, N., D. L. Wu and D. R. Themens (2020). Comparison and evaluation of a bottom-up GPS-RO electron density retrieval for D and E regions using radar observations and models, J. Atmos. Sol.-Terr. Phys., 207, 105333, doi:10.1016/j.jastp.2020.105333.

Tahir, A., F. Wu, M. Shah, C. Amory-Mazaudier et al. (2024). Multi-instrument observation of the ionospheric irregularities and disturbances during the 23-24 March 2023 geomagnetic storm, Remote Sens., 16, 1594, doi:10.3390/rs16091594.

Van Dierendonck, A. J., J. Klobuchar and Q. Hua (1993). Ionospheric scintillation monitoring using commercial single frequency C/A code receivers, Proc. ION GPS-93, 1333-1342.

Whitehead, J. D. (1961). The formation of the sporadic-E layer in the temperate zones, J. Atmos. Terr. Phys., 20, 1, 49-58, doi:10.1016/0021-9169(61)90097-6.

Whitehead, J. D. (1989). Recent work on mid-latitude and equatorial sporadic E, J. Atmos. Terr. Phys., 51, 401-424, doi:10.1016/0021-9169(89)90122-0.

Wu, D. L., C. O. Ao, G. A. Hajj, M. T. Juarez and A. J. Mannucci (2005). Sporadic E morphology from GPS-CHAMP radio occultation, J. Geophys. Res. Space Phys., 110, A1, A01306, doi:10.1029/2004JA010701.

Xu, X., J. Luo, H. Wang, H. Liu and T. Hu (2022). Morphology of sporadic E layers derived from Fengyun-3C GPS radio occultation measurements, Earth Planets Space, 74, 1-13, doi:10.1186/s40623-022-01617-2.

Yamauchi, M., T. Kotani, S. Nanjo and J. Matzka (2025). UT dependence of severe space weather events defined by geomagnetic indices: An unusual aspect of the May 2024 event, Earth Planets Space, 77, doi:10.1186/s40623-025-02292-9.

Yamazaki, Y., J. Matzka, C. Stolle, G. Kervalishvili et al. (2022). Geomagnetic activity index Hpo, Geophys. Res. Lett., 49, doi:10.1029/2022GL098860.

Yan, X., H. Cai, L. Qiu, J. Zhou et al. (2025). Height and intensity variations of mid-latitude sporadic E-layers observed by FORMOSAT-3/COSMIC and ionosondes, J. Geophys. Res. Space Phys., 130, e2024JA033378, doi:10.1029/2024JA033378.

Yeh, K. C. and C. H. Liu (1982). Radio wave scintillations in the ionosphere, Proc. IEEE, 70, 4, 324-360, doi:10.1109/PROC.1982.12313.

Yokoyama, T. et al. (2009). Three-dimensional simulation of the coupled Perkins and Es-layer instabilities in the nighttime midlatitude ionosphere, J. Geophys. Res. Space Phys., 114, doi:10.1029/2008JA013789.

Yokoyama, T., D. L. Hysell, Y. Otsuka and M. Yamamoto (2009). Three-dimensional simulation of the coupled Perkins and Es-layer instabilities in the nighttime midlatitude ionosphere, J. Geophys. Res. Space Phys., 114, doi:10.1029/2008JA013789.

Yu, B., C. J. Scott, X. Xue, X. Yue and X. Dou (2020). Derivation of global ionospheric sporadic E critical frequency (foEs) data from the amplitude variations in GPS/GNSS radio occultations, R. Soc. Open Sci., 7, 7, 200320, doi:10.1098/rsos.200320.

Yu, B., X. Xue, X. Yue, C. Yang et al. (2019). The global climatology of the intensity of the ionospheric sporadic E layer, Atmos. Chem. Phys., 19, 4139-4151, doi:10.5194/acp-19-4139-2019.

Yu, Y., T. Yu, L. Qiu, X. Yan, J. Wang et al. (2023). Comparison of the heights of sporadic E layers and vertical ion convergence parameters, Remote Sens., 15, 5674, doi:10.3390/rs15245674.

Yue, X., W. S. Schreiner, N. Pedatella and Y.-H. Kuo (2015). A case study on complex sporadic E layers observed by GPS radio occultations, Atmos. Meas. Tech., 8, 1, 225-236, doi:10.5194/amt-8-225-2015.

Zeng, Z., S. Sokolovskiy, W. Schreiner and D. Hunt (2019). Representation of vertical atmospheric structures by radio occultation observations in the upper troposphere and lower stratosphere: Comparison to high-resolution radiosonde profiles, J. Atmos. Oceanic Technol., 36, 4, 655-670, doi:10.1175/jtech-d-18-0105.1.

***CORRESPONDING AUTHOR: Mefe MOSES**,
Ahmadu Bello University Zaria, Department of Geomatics, Kaduna, Nigeria
e-mail: mosesmefe@gmail.com